

Graphene supported double-layer carbon encapsulated silicon for high-performance lithium-ion battery anode materials

Yanhong Lu^{a,*}, Zhantong Ye^a, Yating Zhao^a, Qing Li^a, Meiyu He^a, Congcong Bai^a, Xiaotong Wang^a, Yalu Han^a, Xingchen Wan^a, Suling Zhang^a, Yanfeng Ma^{b,**}, Yongsheng Chen^b

^a School of Chemistry & Material Science, Langfang Normal University, Langfang, 065000, China

^b The Centre of Nanoscale Science and Technology and Key Laboratory of Functional Polymer Materials, State Key Laboratory and Institute of Elemento-Organic Chemistry, College of Chemistry, Nankai University, Tianjin, 300071, China

ABSTRACT

Carbon coating has been an effective procedure to tackle the severe structural degradation and poor conductivity during cycling of silicon-based anodes in lithium-ion batteries (LIBs). However, the traditional coated carbon usually is tight and thus limit the fast-charging rate and high specific capacity. Herein, through in-situ formation of metal-organic frameworks on the surface, silicon particles were firstly coated by an inside carbon layer. Followed by a solvothermal reaction with the mixture of sucrose and graphene oxide, the second carbon layer outside the silicon particles was deposited, and simultaneously a highly conductive graphene network was formed. After a high temperature pyrolysis process, a graphene matrix supported silicon material with inward multi-channel carbon and outward tight activated carbon was prepared. This unique core/double-layer carbon structure, combined with the highly conductive graphene frameworks, render the material to demonstrate excellent electrochemical performance as anode materials for LIBs in terms of both lithium storage capacity and cycling stability. Thus, the electrode materials deliver a high specific capacity of 1528.1 mA h g⁻¹ at the current density of 0.1 A g⁻¹ and rate capacity retention of 45.5% at 1 A g⁻¹ to 0.1 A g⁻¹. Simultaneously, a highly stable reversible capacity of 1182 mAh g⁻¹ with 89.5% retention over 240 cycles at a current density of 0.2 A g⁻¹ and 484 mAh g⁻¹ with 76.8% retention after 450 cycles at 1.0 A g⁻¹ were obtained. This work can offer an alternative approach for high-energy and low-cost silicon-based anodes for LIBs.

1. Introduction

Lithium-ion batteries (LIBs) with excellent energy density and superior cycling life have become the most important energy storage technology for electric vehicles, portable electronics and renewable energy storage [1]. Silicon, owing to its highest theoretical capacity (~4200 mA h g⁻¹), a relatively lower discharge voltage (<0.5 V vs. Li⁺/Li) and abundance in nature [2–4], has been considered as one of the most promising candidates as the anode materials for LIBs. However, silicon undergoes a huge volume change (>300%) during the repeated charge/discharge cycles. This causes dramatic pulverization of silicon particles and thus leads to unceasing formation of solid-electrolyte interphase film on the surface of silicon and rapid capacity attenuation upon cycling [5,6]. Furthermore, the low intrinsic electrical conductivity of pristine silicon significantly suppresses its charge/discharge behaviors. To overcome these obstacles, the strategy of encapsulation of silicon with conductive carbon coating layers has been well developed [7,8]. In such carbon coated silicon materials, the carbon shell/sheath

could work as a protective layer for buffering the volume expansion of silicon particles, prevent them from directly contacting with the electrolyte, in addition to enhancing the materials' conductivity [9,10]. Therefore, the carbon encapsulated silicon can provide much improved mechanical tolerance to achieve better charge/discharge cycling and rate performance [11,12].

Carbon derived from various precursors, such as pitch [13,14], pyridine [15], chitosan [16], biomass [17], polymers [18–24], hydrocarbon gases [25] and so on, have been widely used as the coating shell/sheath to improve the structural and electrical performance of such silicon composites. Various metal-organic frameworks (MOFs), consisting of porous carbon frameworks with metal centers, have attracted much interests as the precursors for preparing various anode materials for LIBs due to their diverse morphologies, high porosity and controllable chemical structures [26–28]. Fabrication of core/sheath structures with carbon derived from MOFs encapsulating silicon nanoparticles provides a new pathway to high-performance LIBs anode materials. One-layer carbon derived from zeolitic imidazolate

* Corresponding author.

** Corresponding author.

E-mail addresses: luyanhong@lfnu.edu.cn (Y. Lu), yanfengma@nankai.edu.cn (Y. Ma).

<https://doi.org/10.1016/j.carbon.2022.10.010>

Received 11 February 2022; Received in revised form 30 September 2022; Accepted 6 October 2022

Available online 11 October 2022

0008-6223/© 2022 Elsevier Ltd. All rights reserved.

framework (ZIF) coated silicon composites has been synthesized through a grinding and subsequently carbonization process by Wang's group [29], a high voltage sputtering process by Liu et al. [30], a stirring with followed carbonization process by Li et al. [31], and growing ZIF-8 on benzoic acid-functionalized nano-Si with subsequent pyrolyzation process by Song et al. [32]. In addition, Wang et al. constructed a novel porous silicon microsphere, coated by one-layer carbon derived from MOFs and consisting of numerous interconnected nanowires, manifested an enhanced lithium storage performance [33].

Meanwhile, double-layer carbon coated silicon materials as anode materials have been also investigated. For example, silicon anode materials with silicon/carbon yolk/shell structure have been fabricated, where polystyrene was used as the precursor generating pores and inner carbon sheath, and polyaniline was used as the source for outer carbon sheath [34]. Amorphous/crystalline dual carbon coated silicon nanoparticles have been synthesized by various methods, including pyrolyzing [35,36], ball-milling [37], liquid coating followed by polymerization process [38], carbonization of MOFs with polymer [39] and so on. Recently, a multifunctional composite, where silicon nanoparticles embedded in macro-porous carbon and then coated with an outer amorphous carbon, was prepared through carbon coating, carbonization, pore-creating, silicon deposition and the outer amorphous carbon formation [40]. The inner macro-porous matrix with high silicon content provides sufficient pores to alleviate the volume change of silicon, meanwhile, the outer protective carbon layer could endure a high mechanical pressure, limiting the damage during the charge/discharge process.

Furthermore, owing to the excellent structural and electrical properties, graphene has also become a promising candidate to encapsulate silicon nanostructures to construct energetic architectures for high-performance LIBs anode materials [41]. Graphene sheets have been deposited on the surface of silicon spheres/wires through various methods, such as an electrostatic attraction method [1,12], in-situ growth process by chemical vapor deposition [11,42–45], covalent linkage immobilization [46,47] mechanical blending [48], solvent exchange process [49], steam etching [50], and plasma-assisted milling [51,52] and so on.

Moreover, ternary complex based on one-layer carbon coated silicon structures, which were further anchored on high conductive 1D/2D nanowires/nanosheets [53–57] or 3D carbon nanotube foam [2,58,59], graphene spongy [60–62], Ni foam [63], graphite [64] and polymer frameworks [65,66] have been fabricated. Combined with the outstanding conductive abilities of the nanoscale matrix, the silicon composites exhibit excellent structural and interfacial stability, as well as enhanced capacity and cycling stabilities.

While carbon coating and introduction of highly conductive matrix are popular strategies for improvement of the lithium storage capacity, nevertheless, less attentions have been given for the carbon layer with optimal channels for lithium-ion transport. Furthermore, very limited works have been carried out on the silicon anode materials with a double-layer carbon coating structure, and no such work with the introduction of high conductive graphene as the matrix to provide a plat for silicon nanoparticles has been reported.

In this work, as shown in Fig. 1, an anode silicon material with a double-layer carbon coating structure, named as Graphene/IOC@Si, was fabricated, where the highly conducting graphene was used as the matrix to anchor the silicon particles which were first encapsulated with a MOFs derived inward carbon shell, and then sucrose derived outward carbon layer. Here, ZIF-8 was firstly assembled on the silicon surface to obtain ZIF-8 encapsulated silicon nanoparticles, denoted as ZIF-8@Si. Then this ZIF-8@Si was coated with sucrose and deposited on graphene sheets through ball-milling, followed by a solvothermal reaction and pyrolysis process. With graphene network formed in the solvothermal process, a ternary composite of Graphene/IOC@Si was fabricated. Different from the traditional coated carbon, the MOFs derived carbon preserved the unique multi-channel of the framework, which can not only effectively buffer and accommodate the volume expansion of silicon, but also greatly promote the infiltration of the electrolyte ions to the anode. The outward sucrose produced activated carbon with tight structure acting as the second buffer shell/sheath can further relax the volume change of the inner particles. Meanwhile, the graphene matrix associated with interconnected networks can provide sufficient space to accelerated silicon nanoparticles, along with the electrolyte ions and simultaneously render an excellent electrical conductivity for the whole anode materials. As consequence, the unique Graphene/IOC@Si anode materials exhibit a high lithium storage specific capacity up to 1528.1 mA h g⁻¹ at the current density of 0.1 A g⁻¹, as well as enhanced rate capability and excellent cycling stability.

2. Experimental

2.1. Materials synthesis

All the chemicals used in this work are analytical grade and there is no other treatment. Deionized water was used in all experiments. Graphene oxide (GO) was purchased from Tianjin Plannano Energy Technologies Co., Ltd.

In-situ growth ZIF-8 on silicon nanoparticles was first performed by a simply ball milling process with precursors of forming ZIF-8 and silicon nanoparticles in solvent. Typically, silicon powder (30 mg, Shanghai Aladdin Biochemical Technology Co., Ltd.) with average diameter of ~60 nm was firstly dispersed in methanol (10 mL) by ultrasonic, and then was ball-milled for 1 h at 500 rpm. After that, Zn(NO₃)₂·6H₂O (1.0 g) solution in methanol (5 mL) and 2-methylimidazole (1.6 g) solution in methanol (5 mL) were added respectively and continued to ball-mill for another 1 h at 500 rpm. After this process, the intermediate products were separated by centrifuge at 1000 rpm for 15 min. The sediments were collected and thoroughly washed with methanol and then dried in a vacuum oven at 120 °C for 12 h to generate the ZIF-8 coated silicon nanoparticles, named ZIF-8@Si. The obtained ZIF-8@Si was then mixed with GO aqueous solution (3 mg mL⁻¹, 10 mL) and sucrose aqueous solution (130 mg mL⁻¹, 10 mL) and continued to ball-milling for 3 h at 500 rpm. After another stirring for 12 h at room temperature, the above dispersion was then applied with a hydrothermal process and followed carbonization step according to our previous approaches [67,68]. Briefly, the homogeneous mixture was firstly transferred to an autoclave

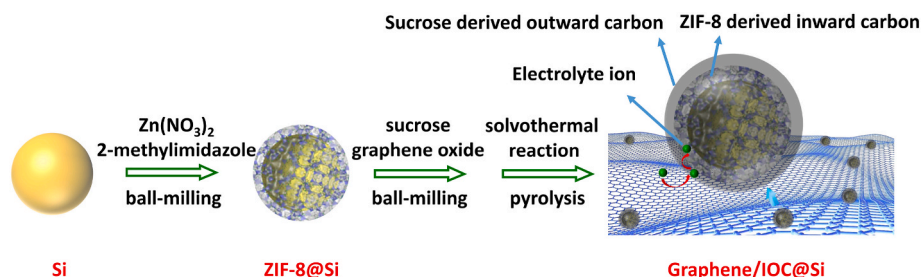


Fig. 1. Schematic of the fabrication process of Graphene/IOC@Si. (A colour version of this figure can be viewed online.)

(100 mL), heated to 200 °C and kept for 12 h. After that, the hydrothermal product was vacuum filtered, thoroughly washed with distilled water, and dried in a vacuum oven at 120 °C for 24 h. Finally, the sample was collected and placed in a nickel boat and heated to 800 °C at the rate of 5 °C min⁻¹ under Ar/H₂ atmosphere (5% H₂) in a horizontal tube furnace, which was kept for 1 h at that temperature and the Graphene/IOC@Si materials were obtained.

As comparison, the control sample, without ZIF-8, only with sucrose derived single carbon layer coated silicon nanoparticles dispersed on graphene sheets (Graphene/C@Si) was also synthesized and compared at the same conditions as that of Graphene/IOC@Si. Another two control samples, different loading of GO and sucrose mass were also studied in the hydrothermal reaction solution, and the products named Graphene/IOC@Si-2GO (with a doubled GO loading, 6 mg mL⁻¹, 10 mL) and Graphene/IOC@Si-2Sucrose (with a doubled sucrose loading, 260 mg mL⁻¹, 10 mL), respectively. For further comparison, ZIF-8@Si was carbonized in a horizontal tube furnace under the same conditions with at 800 °C under Ar/H₂ atmosphere (5% H₂) for 1 h, and the product was named ZIF-8@Si-C as another control sample.

2.2. Characterization

X-ray diffraction (XRD) was performed using a Rigaku D/Max-2500 diffractometer with Cu K α radiation. Raman spectra were examined with a Renishaw InVia Raman spectrometer with laser excitation at 514.5 nm. Lorentzian fitting was used to confirm the positions and the full width at half maximum (FWHM) of the D and G bands. Scanning electron microscopy (SEM) was carried out on a Phenom Pro SEM (For Graphene/IOC@Si sample) and Zeiss Gemini SEM 300 (For Graphene/C@Si sample). Transmission electron microscopy (TEM) and high-resolution transmission electron microscopy (HR-TEM) images were obtained on a FEI Tecnai G2 F20 electron microscope with an acceleration voltage of 200 kV. X-ray photoelectron spectroscopy (XPS) analysis was conducted on an AXIS HIS 165 spectrometer using a monochromatized Al K α X-ray source (1486.7 eV). The thermogravimetric analysis (TGA) and differential thermal analysis (DTA) were tested on a TA Q600 apparatus from room temperature to 900 °C at a heating rate of 10 °C min⁻¹ in air. Inductively coupled plasma optical emission spectroscopy (ICP-OES, Agilent 725) was used to analyze Zn content in Graphene/IOC@Si sample.

2.3. Fabrication of LIBs and electrochemical measurements

The electrochemical performance of the samples was studied based on a typical CR2032 coin-type half-cell in an argon-filled glove box. The working electrode was prepared with 70 wt% active material, 10 wt% conductivity agent Super P, together with 20 wt% polyvinylidene fluoride dissolved in N-methyl-2-pyrrolidone as a binder. The electrode materials were well mixed and then coated onto a copper foil. After dried in a vacuum oven at 180 °C for 6 h, the sheet was punched into rounded electrodes with 10 mm diameter, and the loading mass of active materials was 1.0–1.4 mg. Lithium metal foils and Celgard 2325 membrane were used as the counter electrode and separator, respectively. The electrolyte was the solution of 1 M LiPF₆ dissolved in the mixture of ethylene carbonate/diethyl carbonate (1:1, v/v) with 5 wt% fluoroethylene carbonate additive, and 60 μ L electrolyte was used for each cell.

All the electrochemical tests were performed at room temperature. Galvanostatic charge-discharge cycle tests were conducted on a LAND battery testing system (LAND CT2001A model, Wuhan LAND Electronics. Ltd.) with a potential range of 0.005–1.5 V (vs. Li⁺/Li) at various current densities. Using an electrochemical workstation (P4000, Princeton, USA), cyclic voltammetry (CV) measurements were recorded between 0.005 and 1.5 V (vs. Li⁺/Li), and electrochemical impedance spectroscopy (EIS) was measured by applying a 10 mV amplitude signal in the range of 100 kHz to 10 mHz. The galvanostatic intermittent

titration technique (GITT) measurements were conducted using the LAND CT2001A battery tester from 0.02 to 1.5 V with a pulse current of 0.1 A g⁻¹ applied for 10 min and with a 10 min rest interval.

For comparison, the electrochemical performance of the control samples was also investigated with the same test method.

3. Results and discussion

3.1. Structure and morphology characterization

In order to achieve excellent performance of silicon composites, it is critical to obtain well dispersed silicon nanoparticles with stable structure during the charge/discharge process. This requires controlling well not only the carbon coating but also the dispersibility of the silicon nanoparticles in the composite. Therefore, ZIF-8 and sucrose were selected as the inner and outer coating carbon source respectively. Simultaneously, graphene sheets, with excellent structural properties and remarkable electrical conductivity, were introduced as a support matrix of the silicon nanoparticles to enhance the electrochemical performance.

ZIF-8 was firstly in-situ synthesized on the nano silicon surface through simple ball milling process, denoted as ZIF-8@Si. As designed and expected, ZIF-8 framework coating silicon particles were obtained. As shown in Fig. 2a, the distorted cubic (direction of arrows 1 and 2) and similar sodalite structural ZIF-8@Si (direction of arrow 3) particles are clearly presented. Noted that some individual silicon particles were also observed in the SEM image. For these silicon particles, while the perfect ZIF-8 frameworks outside might not form, whereas, some precursor-like of the carbon layer maybe still exist on the surface of these silicon particles, which could still produce the designed inner carbon layer after carbonization at high temperature. The XRD results of ZIF-8@Si (Fig. 2b) demonstrates a typical pattern of crystal structure of ZIF-8 (marked with “#”), which is accordance with the standard XRD of ZIF-8, indicating that ZIF-8 was formed in the ball milling process. Simultaneously, the peaks of silicon are obvious in the XRD results of ZIF-8@Si (marked with “*”). After carbonization at high temperature, a carbon-coated (derived from ZIF-8) silicon material ZIF-8@Si-C was obtained. In the XRD results, the characteristic peaks of ZIF-8 disappeared while the silicon peaks become intensified, indicating the skeleton of ZIF-8 was collapsed during the pyrolysis process and amorphous carbon formed. To obtain the outer carbon layer, sucrose was then introduced together with the graphene oxide to the ZIF-8@Si dispersed aqueous solution. After a solvothermal reaction and following carbonization process at high temperature, sucrose formed the outward carbon layer outside the inner carbon layer on the surface of silicon particles. Meanwhile, during the process the graphene framework works simultaneously as a matrix support to anchor the double-layer carbon coated silicon nanoparticles. In the XRD pattern of the final product Graphene/IOC@Si composite (Fig. 2b), after coating with sucrose and depositing on graphene matrix and then pyrolysis, all the peaks of ZIF-8 phase disappeared, while the peaks assigned to the crystalline silicon emerged. The diffraction peaks at 28.7°, 47.5°, and 56.3° indexed to the (111), (220), and (331) lattice planes of crystalline silicon (JCPDS No. 27–1402), respectively [61,69]. The broad and weak diffraction peak at about 25° in the XRD patterns of Graphene/IOC@Si are ascribed to the (002) plane of lower ordering reductive graphene oxide (rGO), formed in the hydrothermal and pyrolysis process [70]. The characteristics of the silicon crystal and highly disordered carbon are also manifested by the Raman results. In Fig. 2c, the characteristic peak of silicon crystal at 515 cm⁻¹ was observed [69]. Meanwhile, the D band at 1359 cm⁻¹ and G band at 1591 cm⁻¹, attributing to the disordered carbon crystallites and crystalline graphite respectively, were also presented. Based on the FWHM values of D and G bands (~224 and 81 respectively), a high ratio of D and G bands ($I_D/I_G = 2.76$) was obtained, illustrating a high degree of structural disorder graphene sheets and the amorphous carbon derived from ZIF-8 and sucrose.

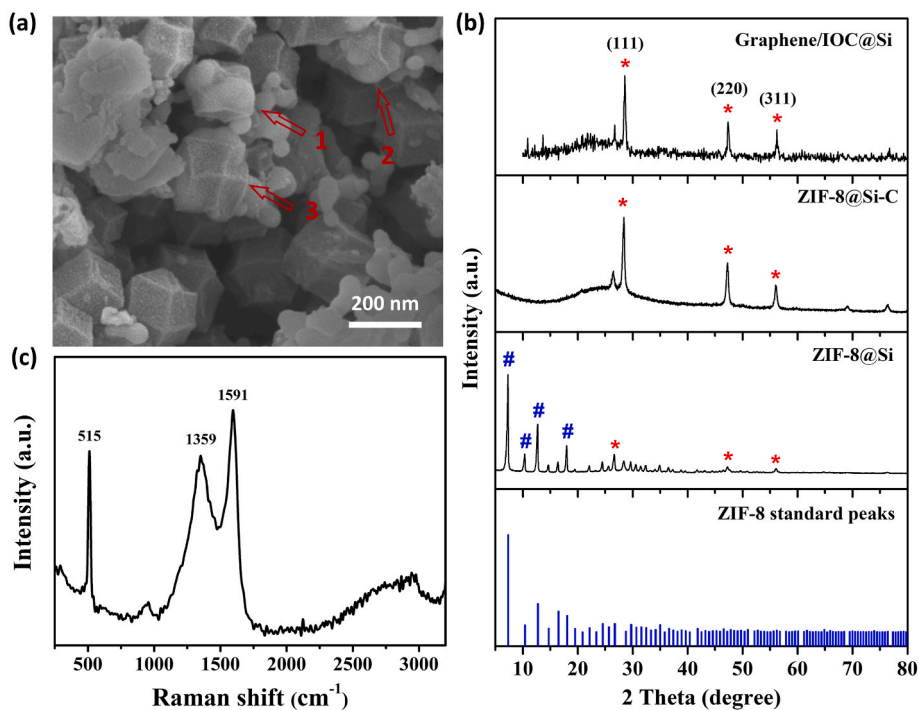


Fig. 2. Morphology and structure analyses of the prepared samples. (a) SEM of ZIF-8@Si sample. (b) XRD results of Graphene/IOC@Si, ZIF-8@Si, ZIF-8@Si-C, and the compared ZIF-8 standard peaks. (c) Raman spectrum of Graphene/IOC@Si sample. (A colour version of this figure can be viewed online.)

The morphology and the microstructure of the final product Graphene/IOC@Si material was also examined through SEM and TEM analyses. As shown in Fig. 3a, the obtained composite has a relatively loose packed and porous foam structure. At a higher magnification (Fig. 3b), the graphene layers can be observed on the surface of the composite, in which silicon nanoparticles are embedded/anchored, forming a graphene matrix supported silicon nanoparticles structure. The TEM image (Fig. 3c) demonstrates that the sphere-shaped silicon nanoparticles with a diameter of about 60 nm are uniformly dispersed on the translucent and wrinkled graphene sheets. As an excellent framework, graphene

sheets not only prevent the silicon nanoparticles from aggregation but also construct electrically conductive networks, greatly improving the electrical conductivity of the whole composite. The HR-TEM image (Fig. 3d) shows the clear (111) planes of crystalline silicon with a d -spacing of 0.31 nm (inset of Fig. 3d), and the crystalline silicon nanoparticle is coated by amorphous carbon layers. Also, in this final product Graphene/IOC@Si, an amorphous carbon layer with a thickness of about 7 nm is clearly exhibited. Based on the carbon layer thickness estimation of the control sample of Graphene/C@Si (without MOFs derived inner carbon layer, Fig. S1), the MOFs derived inner carbon

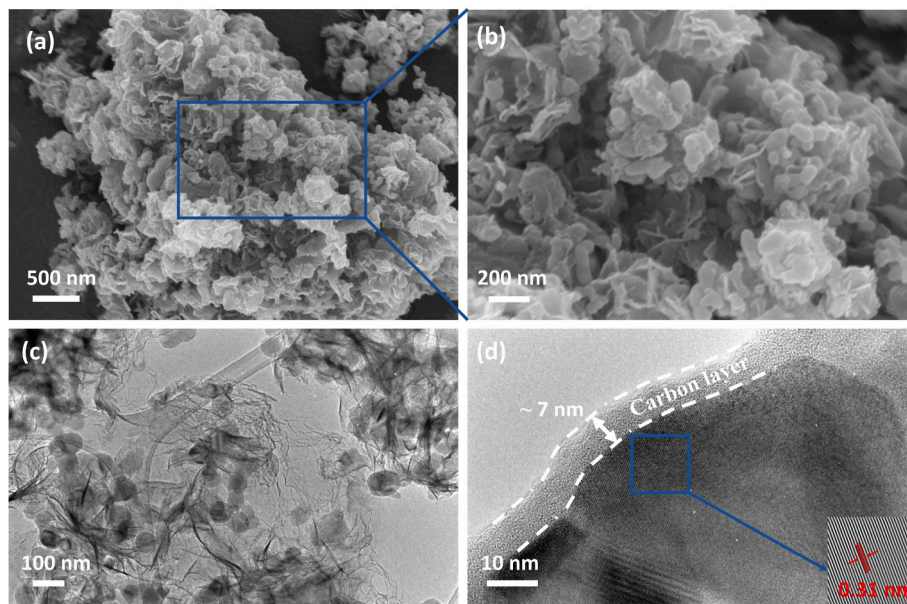


Fig. 3. The morphology and microstructure analyses of Graphene/IOC@Si. (a) SEM image. (b) Magnified SEM image of the rectangle area in (a). (c) TEM image. (d) HR-TEM image of the nano silicon particles coated with amorphous carbon layer marked with white dash, inset is the lattice fringes of the crystalline silicon nanoparticle. (A colour version of this figure can be viewed online.)

layer in Graphene/IOC@Si is estimated with a thickness of about 2 nm. In addition, the carbon layer thickness of the control sample of ZIF-8@Si-C is about 2.4 nm (Fig. S2), supporting that the inner carbon layer with ~2 nm thickness in Graphene/IOC@Si is contributed by MOFs. This double-layer structure with both inner and outer carbon layers offers a better tolerance for the expansion of silicon nanoparticles and thus should improve the structural stability of the electrode materials during the charge/discharge cycling. Note that, the inner porous carbon layer derived from ZIF-8 frame provide favorable paths for transportation of the electrolyte ions, and thus increasing the contact between the inner silicon nanoparticles and the electrolyte ions, desired for a high capacity and rate performance. Furthermore, the carbon layers should also serve as a bridge between silicon nanoparticles and graphene sheets, giving rise to a robust electron transfer way in the case of large volume changes [22].

The chemical composition and surface electronic states of Graphene/IOC@Si composites were investigated by XPS. As shown in Fig. 4a, the survey spectrum demonstrates the coexistence of Si, C, O, as well as Zn, arising from ZIF-8 precursor. The high-resolution Si 2p spectrum (Fig. 4b) exhibits evident peaks at 99.9 and 103.8 eV, which can be attributed to the Si-Si and SiO_x/Si (x < 2) band, respectively [60,61,71]. The formation of SiO_x (x < 2) might be due to the oxidation of silicon nanoparticles with GO under the hydrothermal and thermal treatment. The peaks of silicon with higher oxidation states (such as SiO₂, at ~105 eV) [71] did not appear in Graphene/IOC@Si composites, demonstrating silicon is well preserved. The high-resolution C 1s scanning spectrum (Fig. 4c) is split into three peaks of 284.6, 285.4, and 288.3 eV, which can be assigned to the C-C, C-N and O-C=O bands, respectively [60]. The weaker O-C=O peak indicate some oxygen-containing functional groups appeared on the surface of rGO sheets, which is in accordance with the Raman results. In the high-resolution N 1s spectrum (Fig. 4d), the peaks at 398.3, 400.8 and 402.5 eV are observed, assigning to the pyridinic N, pyrrolic N and graphitic N respectively [60]. The N 1s, along with the C-N band in the high-resolution C 1s, are attributed to the ZIF-8 derived component in the composite. Compared with the final product Graphene/IOC@Si, the control sample of Graphene/C@Si shows different chemical compositions, as shown in Fig. 4e and f. In the survey spectrum, there is no Zn composition due to the absent of ZIF-8 in the precursors for the control sample of Graphene/C@Si. Noted that, the

high-resolution spectrum of Si 2p exhibits the peak of SiO₂ at ~105.0 eV, different from the SiO_x/Si (x < 2) in Graphene/IOC@Si sample, indicating more silicon was oxidized. The relatively low degree of oxidation of silicon in Graphene/IOC@Si can contribute to the introduction of inner carbon derived from ZIF-8, which prevents the silicon nanoparticles from oxidizing during the preparation process.

For quantifying the content of silicon in Graphene/IOC@Si composite, TGA was carried out from room temperature to 900 °C in air. As shown in Fig. S3, an abrupt weight loss of about 63.4% occurs between 500 and 700 °C together with a main exothermic peak at about 580 °C, indicating the oxidation and decomposition of carbon (graphene and double-layer carbon). At 700 °C, the retention of the mass is 36.6.0%, being regarded as the oxidation of Zn and Si with formation of ZnO and SiO₂ respectively. From the ICP-OES analysis, the Zn content is 3.01%. Combined with the weight gain from the oxidation of silicon (TGA curve of pristine silicon is shown in Fig. S4 and the weight gain is 5.5% at 700 °C), thus the content of silicon in Graphene/IOC@Si composites is calculated to be 31.2 wt%.

3.2. Electrochemical performance

The coin-type half-cell was assembled with Graphene/IOC@Si and lithium metal foil as the working and counter electrodes respectively, and the electrochemical performance was studied. The initial five CV curves of Graphene/IOC@Si electrode are shown in Fig. 5a. In the first cathodic scan curve, the reduction peaks at 0.3–1.2 V are related to the formation of solid electrolyte interphase (SEI) films, arising from the reaction of the lithium ions with electrolytes as well as the decomposition of electrolytes on the surface of the electrode material. While, this peak disappears in the subsequent cycles, illustrating that a stable SEI layer formed. The cathodic peak at about 0.2 V formed in the subsequent discharge cycles represents the formation process of lithium silicide alloy phases (Li_xSi), considered as the lithiation process. In the anodic scanning process, the wide peaks at 0.3 V describe the reverse electrochemical reaction, which is ascribed to the phase transition of Li_xSi to amorphous silicon during delithiation process [22,72]. In the subsequent CV cycles, due to the gradual activation of the electrode materials during the lithiation/delithiation process, the area of the anodic peaks increases gradually. From the third cycle CV test, the anodic and

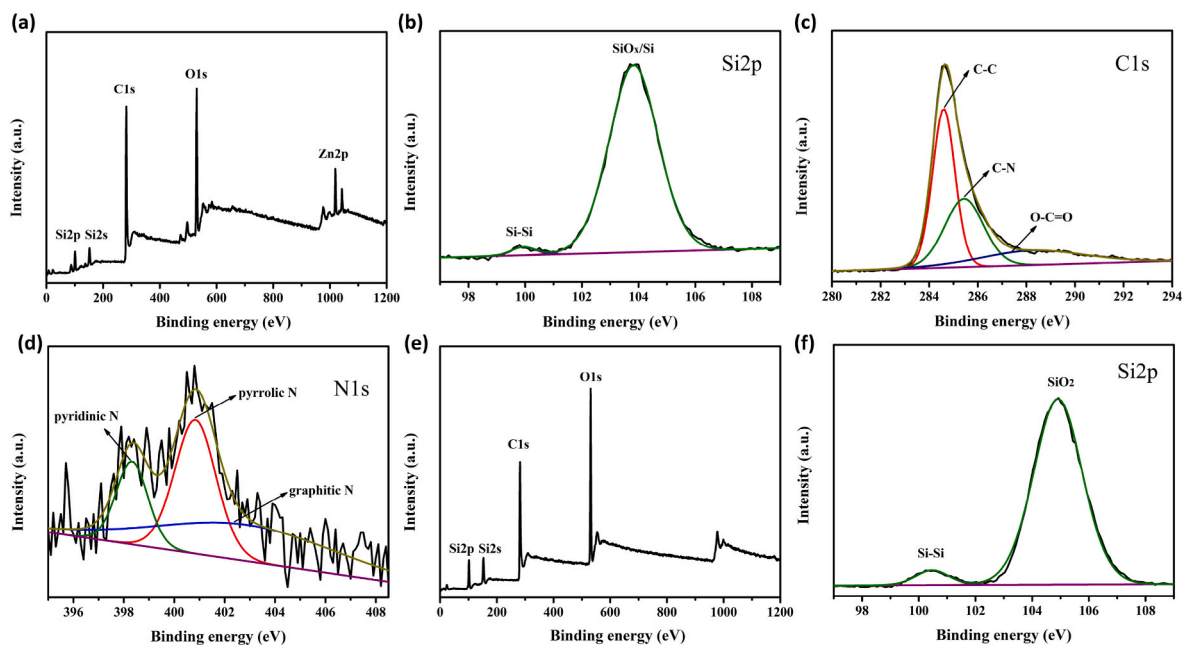


Fig. 4. XPS spectra of (a) survey scan, and high-resolution spectra of (b) Si 2p, (c) C 1s, (d) N 1s for Graphene/IOC@Si. (e) Survey scan and (f) high-resolution spectra of Si 2p for Graphene/C@Si. (A colour version of this figure can be viewed online.)

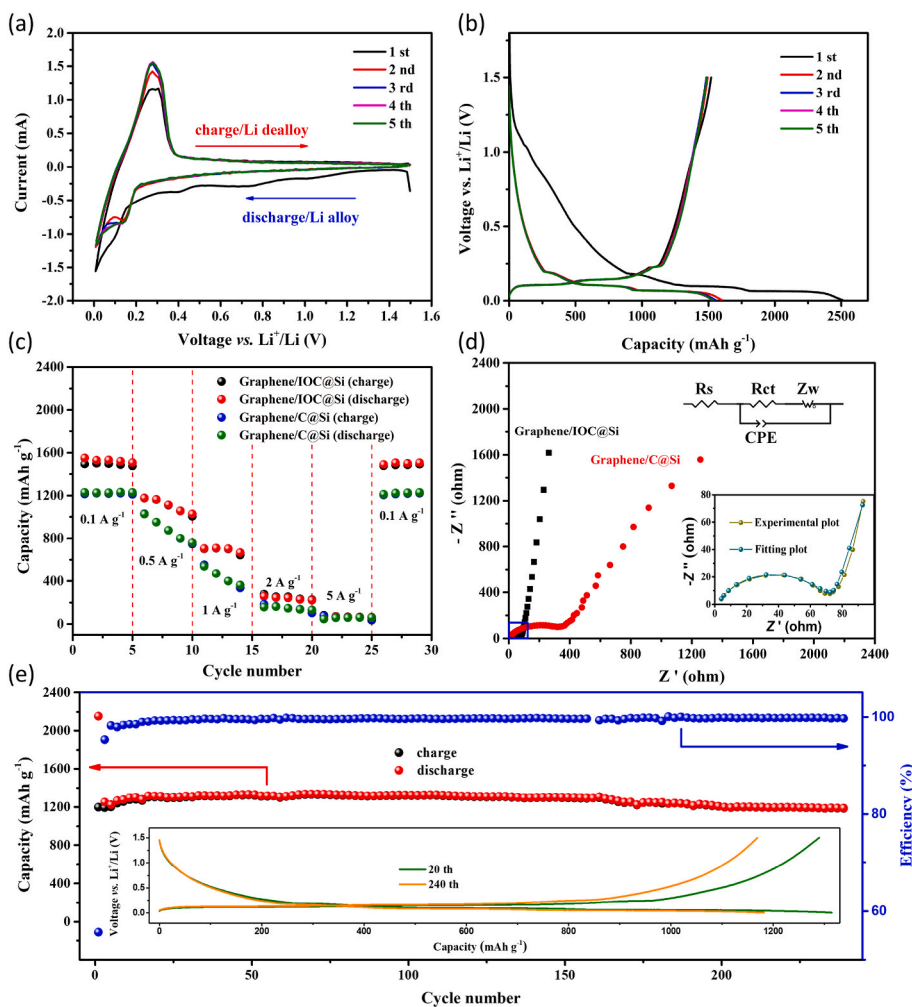


Fig. 5. The electrochemical performance of Graphene/IOC@Si and the control sample of Graphene/C@Si anodes. (a) CV curves of Graphene/IOC@Si with different cycles at 0.1 mV s^{-1} . (b) The initial 5 cycles galvanostatic charge/discharge profiles of Graphene/IOC@Si at 0.1 A g^{-1} in the voltage from 0.005 to 1.5 V. (c) Specific capacity of Graphene/IOC@Si and the control sample of Graphene/C@Si on the current densities from 0.1 to 5 A g^{-1} . (d) Nyquist plots of Graphene/IOC@Si and the control sample of Graphene/C@Si, inset is the electric equivalent circuit and the fitting plots of Graphene/IOC@Si. (e) Cycling stability test of Graphene/IOC@Si at the current density of 0.2 A g^{-1} for 240 cycles with 89.5% specific capacity retention, inset is the charge/discharge profiles of 20th and 240th cycle, respectively. (A colour version of this figure can be viewed online.)

cathodic peaks become overlapped perfectly on both location and intensity, indicating the excellent stability and superior reversibility of the anode materials.

The lithiation/delithiation process and rate performance of Graphene/IOC@Si, along with the control sample of Graphene/C@Si electrodes, were tested by the galvanostatic discharge/charge method. As shown in Fig. 5b, for Graphene/IOC@Si electrode, a slope at 1.20–0.10 V in the first discharge profile was obviously observed, corresponding to the formation of SEI films [72]. The long typical voltage plateau below 0.1 V corresponds to the lithiation process of silicon, whereas the plateau at 0.1–0.25 V in the charge process belongs to the delithiation process. The capacities of 2509.0 and $1520.6 \text{ mAh g}^{-1}$ for discharge and charge in the first profile were achieved respectively, indicating an initial Coulombic efficiency of 60.6%. After several cycles, the curves matched, delivering a stable charge/discharge process.

For the rate performance results, as shown in Fig. 5c, Graphene/IOC@Si materials present average specific discharge capacities of 1528.1, 1106.6, 695.3, 238.8, 62.0 mA h g^{-1} at the current densities of 0.1, 0.5, 1.0, 2 and 5 A g^{-1} , respectively, which are 1.10–1.63 times as high as that of the control sample of Graphene/C@Si (Table S1). When the current density goes back to 0.1 A g^{-1} , the recovered discharge capacity of Graphene/IOC@Si anode reaches to $1500.8 \text{ mA h g}^{-1}$ with a recovery rate of 98.2%. Moreover, Graphene/IOC@Si composite shows excellent specific capacity retention performance. The capacity retention rates of Graphene/IOC@Si electrode reach to 72.4%, 45.5% and 15.6% at the current density of 0.5, 1 and 2 A g^{-1} to 0.1 A g^{-1} respectively, obviously higher than that of the control sample of Graphene/

C@Si (71.7%, 36.0% and 11.9%). Compared with previously reported carbon coated silicon anode materials (Table S2), Graphene/IOC@Si also demonstrates an overall much better lithium storage capacity performance than most related materials, including the specific capacity value and the capacity retention value after many cycles. Moreover, for the lithium storage capacity performance of higher mass of active electrode material loading up to 2.51 mg (surface density of 3.20 mg cm^{-2}), a high capacity of 807.8 mAh g^{-1} at the current density of 0.1 A g^{-1} could be still achieved (Fig. S5). However, due to the increased ion-transfer resistance caused by the thickened electrode, the capacity retentions at higher current density became decreased (Table S3). The outstanding lithium storage capacity and the stable capacity rate performance of Graphene/IOC@Si materials are mainly benefited from the double-layer carbon and the conductive graphene matrix. Firstly, the inner carbon layers on the silicon surface derived from ZIF-8 preserve the unique multi-channels of MOFs framework, which can facilitate the transportation of the electrons and electrolyte ions. This effect contributes to the enhanced capacity and the corresponding capacity retention for Graphene/IOC@Si materials, especially at the low current density. Secondly, the double-layer carbon can effectively inhibit the volume expansion and shrinkage of silicon nanoparticles during the charge/discharge process. Furthermore, graphene frameworks can assemble high dispersed silicon nanoparticles as well as the electrolyte ions, delivering an excellent electrical conductivity and fast charge/discharge abilities [71]. To further evaluate the effects of the carbon layer thickness and graphene matrix, the rate performance of the control samples of Graphene/IOC@Si-2GO with double amount of GO and

Graphene/IOC@Si-2Sucrose with double amount of sucrose were studied, and the results were shown in Fig. S6 and Table S3. For Graphene/IOC@Si-2GO sample, a doubled amount of GO was used as matrix, the thickness of the carbon layers outer silicon nanoparticles was hardly changed as expected. Thus, the capacity didn't show much change as expected. While, due to the possible electrical conductivity improvement from the increased graphene content, the capacity retention performance was slightly improved compared with the Graphene/IOC@Si materials. For the Graphene/IOC@Si-2Sucrose sample, the capacity and the retention were clearly decreased. This is probably attributed to the impeded lithium-ion amount transporting to the surface of silicon particles and the unfavorable lithium-ion diffusion kinetics, due to the thickened outer carbon layer from the double dosage of sucrose.

The Nyquist plots of Graphene/IOC@Si and the control sample of Graphene/C@Si electrodes are obtained from the EIS measurements, as shown in Fig. 5d. With an appropriate electric equivalent circuit (Inset in Fig. 5d), the Nyquist plots were fitted and the kinetic parameters were obtained. In the high-frequency region, both of the electrode materials exhibit small internal resistance (R_s), indicating an excellent electrical conductivity [72]. In the medium-frequency range, the much smaller semicircle of Graphene/IOC@Si electrode indicates a lower charge-transfer resistance (R_{ct}) than that of the control sample. Remarkably, in the low-frequency region, the relatively steeper line of Graphene/IOC@Si material suggests more favorable lithium diffusing into the silicon particle process [73]. The decreased R_{ct} value and advantaged lithium diffusion behaviors of Graphene/IOC@Si materials can be attributed to the inner porous carbon layer on the surface of silicon nanoparticles. The appropriate channels in the inner carbon layer provide a convenient pathway for the charge transfer and ion diffusion during the charge/discharge process, and thus improve the electrochemical performance. Meanwhile, the graphene matrix further promotes the electrical conductivity.

The cycling stability of Graphene/IOC@Si materials was evaluated by galvanostatic charge/discharge at the current density of 0.2 A g^{-1} . As shown in Fig. 5e, the specific capacity maintains a stable trend and the

Coulombic efficiency is close to 100%. Even after 240 cycles, a high specific capacity with 89.5% as well as nearly perfectly reserved galvanostatic charge/discharge profile (inset in Fig. 5e) indicates an excellent life time. At a higher current density of 1.0 A g^{-1} , the capacity still remains at 76.8% after 450 cycles (Fig. S7). The structure and morphology of Graphene/IOC@Si materials after cycling was evaluated. As shown in Fig. S8, the pristine morphology and microstructure of the electrode materials after 450 cycles at the current density of 1 A g^{-1} was well reserved, indicating an excellent stability of the electrode structure. The effective double-layer carbon coating on the surface of silicon and the homogeneous dispersion of the nanoparticles in the graphene matrix is the key factor contributing to the superior cycling stabilities of Graphene/IOC@Si composites.

The lithium storage mechanism and diffusion kinetics were evaluated by CV and GITT analyses, as shown in Fig. 6. The CV curves of Graphene/IOC@Si anode at scan rates of $0.1\text{--}0.5 \text{ mV s}^{-1}$ in Fig. 6a show two groups of anodic (Peak A) and cathodic (Peak B) peaks, respectively. For the lithium storage mechanism, the capacity can be contributed from capacitive and/or diffusion ones, which can be analyzed based on a functional relationship between the scan rate (ν) and peak current (i) according to equation (1) [74,75].

$$i = a \nu^b \quad (1)$$

where a is a constant, and b can be obtained from the slope of the fitting straight line of $\log(i)$ vs. $\log(\nu)$. In general, $b = 1$ implies a capacitive contribution process, when $b = 0.5$ represents a diffusion contribution process. According to the CV results in Fig. 6a, the b values of peaks A and B were calculated and was 0.47 and 0.54 respectively (Fig. 6b). The b values of both peaks A and B are close to 0.5, demonstrating a diffusion-controlled charge storage kinetics process for the Graphene/IOC@Si anode.

The lithium-ion diffusion kinetics of Graphene/IOC@Si and the control sample of Graphene/C@Si materials were evaluated by the GITT result. As shown in Fig. 6c, a stable discharging with a consecutive sharp increase of overpotential process was presented in the profiles for these

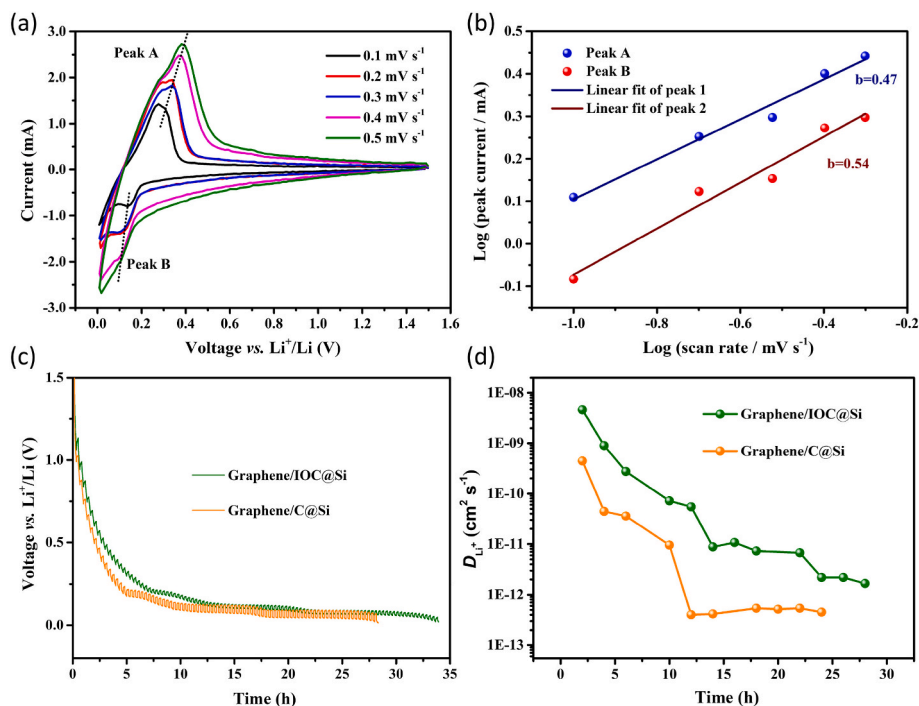


Fig. 6. Kinetic analysis of the lithium-ion storage behaviors. (a) CV curves of Graphene/IOC@Si anode at scan rates of $0.1\text{--}0.5 \text{ mV s}^{-1}$. (b) Fitted lines and $\log(\text{peak current})$ vs. $\log(\text{scan rate})$ plots at peak A and peak B in (a). (c) GITT potential profiles of Graphene/IOC@Si and Graphene/C@Si anodes during lithiation process. (d) The calculated lithium-ion diffusion coefficients according to the discharge profiles in (c). (A colour version of this figure can be viewed online.)

two materials. Compared with the diffusivity curves of the control sample, Graphene/IOC@Si exhibited a relatively smaller overpotential of ~25 mV, confirming a lower electrochemical reaction resistance, consistent with the EIS analysis. Furthermore, the lithium-ion diffusion coefficient (D_{Li}^+) was calculated according to the potential profiles in Fig. 6c based on equation (2) [75,76]:

$$D_{Li^+} = \frac{4}{\pi} \left(\frac{m_B V_M}{M_B S} \right)^2 \left(\frac{\Delta E_s}{\Delta E_\tau} \right)^2 \quad (2)$$

where τ presents the time of the current pulse, and m_B , M_B , V_M indicates the mass, molar mass and molar volume of the active material, respectively. S corresponds to the surface area of the electrode. ΔE_s is the steady-state voltage variation during a single GITT titration. ΔE_τ is the total voltage variation during the current pulse τ of a single GITT titration. The D_{Li}^+ of Graphene/IOC@Si and the control Graphene/C@Si anode was estimated, as shown in Fig. 6d. Graphene/IOC@Si delivers a higher lithium-ion diffusion coefficient of $4.63 \times 10^{-9} - 1.67 \times 10^{-12}$ during the lithiation process, which is higher than that of the control Graphene/C@Si anode ($4.43 \times 10^{-10} - 3.98 \times 10^{-13}$), indicating a faster lithium-ion storage kinetics.

Based on the diffusion-controlled lithium-ion behavior from the CV and GITT analyses, the excellent lithium storage capacity performance of Graphene/IOC@Si can be confirmed. The double carbon layers, especially the porous inner carbon layer extremely facilitate the diffusion. In addition, the lower of the current density, the more obvious of the diffusion behavior. This can be verified from the rate performance in above Fig. 5c. At relatively lower current density of 0.1, 0.5 and 1 A g⁻¹, Graphene/IOC@Si displays obviously higher specific capacity than that of the control Graphene/C@Si anode, and simultaneously delivering higher capacity retention from 0.1 to 1 A g⁻¹.

4. Conclusion

In summary, Graphene/IOC@Si anode material consisting of double-layer carbon coated silicon nanoparticles dispersed uniformly into graphene frameworks were successfully synthesized. The inner carbon layer derived from in-situ MOFs provides adequate channels for the electron and ion transportation. The sucrose derived outer carbon layer restrains the volumetric effect of silicon nanoparticles. The graphene matrix provides sufficient space to disperse and anchor silicon nanoparticles, accelerates the electrolyte ions and simultaneously contribute a stable conductive network. The analysis on lithium storage mechanism and diffusion kinetics shows that the designed double-layer carbon, especially the inner carbon layer, effectively facilitates the lithium-ion diffusion into silicon surface. Therefore, as a LIBs anode material, Graphene/IOC@Si composite exhibits high specific capacity, outstanding rate capability and superior cycling stability. The materials and the preparation method investigated in this work can be easily implemented for large-scale production of the high-performance silicon-based LIBs electrode materials.

CRedit authorship contribution statement

Yanhong Lu: Project administration, Funding acquisition, Supervision, Writing – original draft, Writing – review & editing. **Zhantong Ye:** Methodology, Formal analysis, Data curation. **Yating Zhao:** Methodology, Preparation, Data curation. **Qing Li:** Preparation, Formal analysis. **Meiyu He:** Preparation, Data curation. **Congcong Bai:** Preparation, Data curation. **Xiaotong Wang:** Investigation, Data curation. **Yalu Han:** Preparation, Investigation. **Xingchen Wan:** Preparation, Data curation. **Suling Zhang:** Preparation, Formal analysis. **Yanfeng Ma:** Methodology, Supervision, Writing – review & editing. **Yongsheng Chen:** Methodology, Writing – review & editing, Resources.

Declaration of competing interest

The authors declare that they have no known competing financial interests or personal relationships that could have appeared to influence the work reported in this paper.

Acknowledgements

The authors gratefully acknowledge the financial support from the National Natural Science Foundation of China (NSFC, 51502125), the Natural Science Foundation of Hebei Province of China (E2020408004, B2022408005), the Fundamental Research Funds for the Universities in Hebei Province (JYT201901), the Hebei Higher Education Teaching Reform Research and Practice Project (2019GJJG357), the Undergraduate Innovation and Entrepreneurship Training Program of Hebei Province (202110100001) and the Science and Technology Project of Hebei Education Department (QN2022145).

Appendix A. Supplementary data

Supplementary data to this article can be found online at <https://doi.org/10.1016/j.carbon.2022.10.010>.

References

- [1] X. Zhou, Y.-X. Yin, L.-J. Wan, Y.-G. Guo, Self-assembled nanocomposite of silicon nanoparticles encapsulated in graphene through electrostatic attraction for lithium-ion batteries, *Adv. Energy Mater.* 2 (9) (2012) 1086–1090.
- [2] X. Zhou, Y. Liu, C. Du, Y. Ren, T. Mu, P. Zuo, et al., Polyaniline-encapsulated silicon on three-dimensional carbon nanotubes foam with enhanced electrochemical performance for lithium-ion batteries, *J. Power Sources* 381 (2018) 156–163.
- [3] C.K. Chan, H. Peng, G. Liu, K. McIlwrath, X.F. Zhang, R.A. Huggins, et al., High-performance lithium battery anodes using silicon nanowires, *Nat. Nanotechnol.* 3 (1) (2008) 31–35.
- [4] H. Wu, G. Chan, J.W. Choi, I. Ryu, Y. Yao, M.T. McDowell, et al., Stable cycling of double-walled silicon nanotube battery anodes through solid-electrolyte interphase control, *Nat. Nanotechnol.* 7 (5) (2012) 309–314.
- [5] B. Wang, J. Ryu, S. Choi, X. Zhang, D. Pribat, X. Li, et al., Ultrafast-charging silicon-based coral-like network anodes for lithium-ion batteries with high energy and power densities, *ACS Nano* 13 (2) (2019) 2307–2315.
- [6] N. Liu, Z. Lu, J. Zhao, M.T. McDowell, H.-W. Lee, W. Zhao, et al., A pomegranate-inspired nanoscale design for large-volume-change lithium battery anodes, *Nat. Nanotechnol.* 9 (3) (2014) 187–192.
- [7] K. Xu, X.F. Liu, K.K. Guan, Y.J. Yu, W. Lei, S.W. Zhang, et al., Research progress on coating structure of silicon anode materials for lithium-ion batteries, *ChemSusChem* 14 (23) (2021) 5135–5160.
- [8] Z.D. Chen, L. Li, Z. Zhang, H. Li, B. Xie, Y.G. Chen, et al., “Sticky” carbon coating enables high-area-capacity lithium storage of silicon-graphitic carbon hybrid, *Carbon* 184 (2021) 91–101.
- [9] C.L. Qi, S.P. Li, Z.P. Yang, Z.H. Xiao, L. Zhao, F. Yang, et al., Suitable thickness of carbon coating layers for silicon anode, *Carbon* 186 (2022) 530–538.
- [10] C.H. Huang, Z.J. Feng, F. Pei, A. Fu, B.H. Qu, X.Y. Chen, et al., Understanding protection mechanisms of graphene-encapsulated silicon anodes with operando Raman spectroscopy, *ACS Appl. Mater. Interfaces* 12 (31) (2020) 35532–35541.
- [11] B. Wang, X. Li, X. Zhang, B. Luo, M. Jin, M. Liang, et al., Adaptable silicon-carbon nanocables sandwiched between reduced graphene oxide sheets as lithium ion battery anodes, *ACS Nano* 7 (2) (2013) 1437–1445.
- [12] J. Ji, H. Ji, L.L. Zhang, X. Zhao, X. Bai, X. Fan, et al., Graphene-encapsulated Si on ultrathin-graphite foam as anode for high capacity lithium-ion batteries, *Adv. Mater.* 25 (33) (2013) 4673–4677.
- [13] F. Qu, G. She, J. Wang, X. Qi, S. Li, S. Zhang, et al., Coating nanoparticle-assembled Si microspheres with carbon for anode material in lithium-ion battery, *J. Phys. Chem. Solid.* 124 (2019) 312–317.
- [14] S. Chae, Y.B. Xu, R. Yi, H.S. Lim, D. Velickovic, X.L. Li, et al., A micrometer-sized silicon/carbon composite anode synthesized by impregnation of petroleum pitch in nanoporous silicon, *Adv. Mater.* 33 (40) (2021), 2103095.
- [15] D.K. Wang, C.L. Zhou, B. Cao, Y.C. Xu, D.H. Zhang, A. Li, et al., One-step synthesis of spherical Si/C composites with onion-like buffer structure as high-performance anodes for lithium-ion batteries, *Energy Storage Mater.* 24 (2020) 312–318.
- [16] R. Shao, F. Zhu, Z.J. Cao, Z.P. Zhang, M.L. Dou, J. Niu, et al., Heteroatom-doped carbon networks enabling robust and flexible silicon anodes for high energy Li-ion batteries, *J. Mater. Chem.* 8 (35) (2020) 18338–18347.
- [17] A. Mescerjakovas, K. Murashko, S.M. Alatalo, T. Karhunen, J.T.T. Leskinen, J. Jokiniemi, et al., Influence of induction-annealing temperature on the morphology of barley-straw-derived Si@C and SiC@graphite for potential application in Li-ion batteries, *Nanotechnology* 31 (33) (2020).
- [18] Y. Ouyang, X. Zhu, F. Li, F. Lai, Y. Wu, Y.-E. Miao, et al., Silicon @ nitrogen-doped porous carbon fiber composite anodes synthesized by an in-situ reaction collection

- strategy for high-performance lithium-ion batteries, *Appl. Surf. Sci.* 475 (2019) 211–218.
- [19] Z. Lu, B. Li, D. Yang, H. Lv, M. Xue, C. Zhang, A self-assembled silicon/phenolic resin-based carbon core-shell nanocomposite as an anode material for lithium-ion batteries, *RSC Adv.* 8 (7) (2018) 3477–3482.
- [20] J. Liang, F. Huo, Z. Zhang, W. Yang, M. Javid, Y. Jung, et al., Controlling the phenolic resin-based amorphous carbon content for enhancing cycling stability of Si nanosheets@C anodes for lithium-ion batteries, *Appl. Surf. Sci.* 476 (2019) 1000–1007.
- [21] S.J. Fan, H. Wang, J.F. Qian, Y.L. Cao, H.X. Yang, X.P. Ai, et al., Covalently bonded silicon/carbon nanocomposites as cycle-stable anodes for Li-ion batteries, *ACS Appl. Mater. Interfaces* 12 (14) (2020) 16411–16416.
- [22] G. Liang, X. Qin, J. Zou, L. Luo, Y. Wang, M. Wu, et al., Electrospayed silicon-embedded porous carbon microspheres as lithium-ion battery anodes with exceptional rate capacities, *Carbon* 127 (2018) 424–431.
- [23] M. Ashuri, Q.R. He, L.L. Shaw, Improving cycle stability of Si anode through partially carbonized polydopamine coating, *J. Electroanal. Chem.* 876 (2020), 114738.
- [24] Q. Ma, H.W. Xie, J.K. Qu, Z.Q. Zhao, B.L. Zhang, Q.S. Song, et al., Tailoring the polymer-derived carbon encapsulated silicon nanoparticles for high-performance lithium-ion battery anodes, *ACS Appl. Energy Mater.* 3 (1) (2020) 268–278.
- [25] X.Y. Zhang, B.I. Min, Y.R. Wang, R. Hayashida, M. Tanaka, T. Watanabe, Preparation of carbon-coated silicon nanoparticles with different hydrocarbon gases in induction thermal plasma, *J. Phys. Chem. C* 125 (28) (2021) 15551–15559.
- [26] G.H. Zhang, S.C. Hou, H. Zhang, W. Zeng, F.L. Yan, C.C. Li, et al., High-performance and ultra-stable lithium-ion batteries based on MOF-derived ZnO@ZnO quantum dots/C core-shell nanorod arrays on a carbon cloth anode, *Adv. Mater.* 27 (14) (2015) 2400–2405.
- [27] X. Xu, R. Cao, S. Jeong, J. Cho, Spindle-like mesoporous α -Fe₂O₃ anode material prepared from MOF template for high-rate lithium batteries, *Nano Lett.* 12 (9) (2012) 4988–4991.
- [28] X.C. Xie, K.J. Huang, X. Wu, Metal-organic framework derived hollow materials for electrochemical energy storage, *J. Mater. Chem.* 6 (16) (2018) 6754–6771.
- [29] Y. Han, P. Qi, X. Feng, S. Li, X. Fu, H. Li, et al., In situ growth of MOFs on the surface of Si nanoparticles for highly efficient lithium storage: Si@MOF nanocomposites as anode materials for lithium-ion batteries, *ACS Appl. Mater. Interfaces* 7 (4) (2015) 2178–2182.
- [30] N. Liu, X. Mamat, R. Jiang, W. Tong, Y. Huang, D. Jia, et al., Facile high-voltage sputtering synthesis of three-dimensional hierarchical porous nitrogen-doped carbon coated Si composite for high performance lithium-ion batteries, *Chem. Eng. J.* 343 (2018) 78–85.
- [31] Q. Li, Y. Wang, X. Gao, H. Li, Q. Tan, Z. Zhong, et al., Enhancement of ZIF-8 derived N-doped carbon/silicon composites for anode in lithium ions batteries, *J. Alloys Compd.* 872 (2021), 159712.
- [32] Y. Song, L. Zuo, S. Chen, J. Wu, H. Hou, L. Wang, Porous nano-Si/carbon derived from zeolitic imidazolate frameworks@nano-Si as anode materials for lithium-ion batteries, *Electrochim. Acta* 173 (2015) 588–594.
- [33] K. Wang, S. Pei, Z. He, L.-a. Huang, S. Zhu, J. Guo, et al., Synthesis of a novel porous silicon microsphere@carbon core-shell composite via in situ MOF coating for lithium ion battery anodes, *Chem. Eng. J.* 356 (2019) 272–281.
- [34] X. Huang, X. Sui, H. Yang, R. Ren, Y. Wu, X. Guo, et al., HF-free synthesis of Si/C yolk/shell anodes for lithium-ion batteries, *J. Mater. Chem.* 6 (6) (2018) 2593–2599.
- [35] G. Fang, X. Deng, J. Zou, X. Zeng, Amorphous/ordered dual carbon coated silicon nanoparticles as anode to enhance cycle performance in lithium ion batteries, *Electrochim. Acta* 295 (2019) 498–506.
- [36] J. Chen, X. Guo, M. Gao, J. Wang, S. Sun, K. Xue, et al., Self-supporting dual-confined porous Si@c-ZIF/carbon nanofibers for high-performance lithium-ion batteries, *Chem. Commun.* 57 (81) (2021) 10580–10583.
- [37] Y. Yang, Z.J. Lu, J. Xia, Y. Liu, K. Wang, X. Wang, Crystalline and amorphous carbon double-modified silicon anode: towards large-scale production and superior lithium storage performance, *Chem. Eng. Sci.* 229 (2021), 116054.
- [38] L.H. Zhu, Y.L. Chen, C.Q. Wu, R.X. Chu, J. Zhang, H. Jiang, et al., Double-carbon protected silicon anode for high performance lithium-ion batteries, *J. Alloys Compd.* 812 (2020), 151848.
- [39] D. Jin, B. Saravanakumar, Y.Q. Ou, G.J. Li, W.G. Zhang, H.R. Wang, et al., Highly stabilized silicon nanoparticles for lithium storage via hierarchical carbon architecture, *ACS Appl. Energy Mater.* 3 (5) (2020) 4777–4786.
- [40] Y. Son, N. Kim, T. Lee, Y. Lee, J. Ma, S. Chae, et al., Calendering-compatible macroporous architecture for silicon-graphite composite toward high-energy lithium-ion batteries, *Adv. Mater.* 32 (37) (2020), 2003286.
- [41] X. Zhao, C.M. Hayner, M.C. Kung, H.H. Kung, In-plane vacancy-enabled high-power Si-graphene composite electrode for lithium-ion batteries, *Adv. Energy Mater.* 1 (6) (2011) 1079–1084.
- [42] I.H. Son, J.H. Park, S. Park, K. Park, S. Han, J. Shin, et al., Graphene balls for lithium rechargeable batteries with fast charging and high volumetric energy densities, *Nat. Commun.* 8 (2017) 1561.
- [43] L. Shi, C. Pang, S. Chen, M. Wang, K. Wang, Z. Tan, et al., Vertical graphene growth on SiO microparticles for stable lithium ion battery anodes, *Nano Lett.* 17 (6) (2017) 3681–3687.
- [44] C. Zhang, T.-H. Kang, J.-S. Yu, Three-dimensional spongy nanographene-functionalized silicon anodes for lithium ion batteries with superior cycling stability, *Nano Res.* 11 (1) (2018) 233–245.
- [45] Y.B.A. Mu, M.S. Han, B.K. Wu, Y.M. Wang, Z.W. Li, J.X. Li, et al., Nitrogen, oxygen-codoped vertical graphene arrays coated 3D flexible carbon nanofibers with high silicon content as an ultrastable anode for superior lithium storage, *Adv. Sci.* (2021), 2104685.
- [46] G. Zhao, L. Zhang, Y. Meng, N. Zhang, K. Sun, Decoration of graphene with silicon nanoparticles by covalent immobilization for use as anodes in high stability lithium ion batteries, *J. Power Sources* 240 (2013) 212–218.
- [47] F.M. Hassan, R. Batmaz, J. Li, X. Wang, X. Xiao, A. Yu, Z. Chen, Evidence of covalent synergy in silicon-sulfur-graphene yielding highly efficient and long-life lithium-ion batteries, *Nat. Commun.* 6 (2015) 8597.
- [48] H. Xiang, K. Zhang, G. Ji, J.Y. Lee, C. Zou, X. Chen, et al., Graphene/nanosized silicon composites for lithium battery anodes with improved cycling stability, *Carbon* 49 (5) (2011) 1787–1796.
- [49] D.P. Wong, H.-P. Tseng, Y.-T. Chen, B.-J. Hwang, L.-C. Chen, K.-H. Chen, A stable silicon/graphene composite using solvent exchange method as anode material for lithium ion batteries, *Carbon* 63 (2013) 397–403.
- [50] H. Tang, J. Zhang, Y.J. Zhang, Q.Q. Xiong, Y.Y. Tong, Y. Li, et al., Porous reduced graphene oxide sheet wrapped silicon yielding highly efficient and long-life lithium-ion battery application, *J. Power Sources* 286 (2015) 431–437.
- [51] W. Sun, R. Hu, H. Zhang, Y. Wang, L. Yang, J. Liu, et al., A long-life nano-silicon anode for lithium ion batteries: supporting of graphene nanosheets exfoliated from expanded graphite by plasma-assisted milling, *Electrochim. Acta* 187 (2016) 1–10.
- [52] W. Sun, R. Hu, H. Liu, M. Zeng, L. Yang, H. Wang, et al., Embedding nano-silicon in graphene nanosheets by plasma assisted milling for high capacity anode materials in lithium ion batteries, *J. Power Sources* 268 (2014) 610–618.
- [53] F. Maroni, R. Raccichini, A. Birrozzi, G. Carbonari, R. Tossici, F. Croce, et al., Graphene/silicon nanocomposite anode with enhanced electrochemical stability for lithium-ion battery applications, *J. Power Sources* 269 (2014) 873–882.
- [54] Z. Luo, Q. Xiao, G. Lei, Z. Li, C. Tang, Si nanoparticles/graphene composite membrane for high performance silicon anode in lithium ion batteries, *Carbon* 98 (2016) 373–380.
- [55] H.W. Wang, J.Z. Fu, C. Wang, J.Y. Wang, A.K. Yang, C.C. Li, et al., A binder-free high silicon content flexible anode for Li-ion batteries, *Energy Environ. Sci.* 13 (3) (2020) 848–858.
- [56] W. Xiao, Y.J. Qiu, Q. Xu, J.J. Wang, C. Xie, J.H. Peng, et al., Building sandwich-like carbon coated Si@CNTs composites as high-performance anode materials for lithium-ion batteries, *Electrochim. Acta* 364 (2020), 137278.
- [57] N.W. Ding, Y. Chen, R. Li, J. Chen, C.X. Wang, Z.F. Li, et al., Pomegranate structured C@pSi/rGO composite as high performance anode materials of lithium-ion batteries, *Electrochim. Acta* 367 (2021), 137491.
- [58] C. Shen, X. Fang, M. Ge, A. Zhang, Y. Liu, Y. Ma, et al., Hierarchical carbon-coated ball-milled silicon: synthesis and applications in free-standing electrodes and high-voltage full lithium-ion batteries, *ACS Nano* 12 (6) (2018) 6280–6291.
- [59] H. Zhang, X. Zhang, H. Jin, P. Zong, Y. Bai, K. Lian, et al., A robust hierarchical 3D Si/CNTs composite with void and carbon shell as Li-ion battery anodes, *Chem. Eng. J.* 360 (2019) 974–981.
- [60] D. He, X. Huang, M. Li, Hierarchical C-P(=O)(-O-)(n) (n <= 2)-linked nano-Si/N-doped C/graphene porous foam as anodes for high-performance lithium ion batteries, *Carbon* 141 (2019) 531–541.
- [61] P. Chang, X. Liu, Q. Zhao, Y. Huang, Y. Huang, X. Hu, Constructing three-dimensional honeycombed graphene/silicon skeletons for high-performance Li-ion batteries, *ACS Appl. Mater. Interfaces* 9 (37) (2017) 31879–31886.
- [62] B. Lee, T. Liu, S.K. Kim, H. Chang, K. Eom, L. Xie, et al., Submicron silicon encapsulated with graphene and carbon as a scalable anode for lithium-ion batteries, *Carbon* 119 (2017) 438–445.
- [63] J. Chang, X. Huang, G. Zhou, S. Cui, P.B. Hallac, J. Jiang, et al., Multilayered Si nanoparticle/reduced graphene oxide hybrid as a high-performance lithium-ion battery anode, *Adv. Mater.* 26 (5) (2014) 758–764.
- [64] Q.H. Nguyen, I.T. Kim, J. Hur, Core-shell Si@c-PAN particles deposited on graphite as promising anode for lithium-ion batteries, *Electrochim. Acta* 297 (2019) 355–364.
- [65] G. Mu, Z. Ding, D. Mu, B. Wu, J. Bi, L. Zhang, et al., Hierarchical void structured Si/PANI/C hybrid anode material for high-performance lithium-ion batteries, *Electrochim. Acta* 300 (2019) 341–348.
- [66] H. Mi, F. Li, C. He, X. Chai, Q. Zhang, C. Li, et al., Three-dimensional network structure of silicon-graphene-polyaniline composites as high performance anodes for Lithium-ion batteries, *Electrochim. Acta* 190 (2016) 1032–1040.
- [67] Y. Lu, S. Zhang, J. Yin, C. Bai, J. Zhang, Y. Li, et al., Mesoporous activated carbon materials with ultrahigh mesopore volume and effective specific surface area for high performance supercapacitors, *Carbon* 124 (2017) 64–71.
- [68] Y. Lu, Y. Yang, T. Zhang, Z. Ge, H. Chang, P. Xiao, et al., Photoprompted hot electrons from bulk cross-linked graphene materials and their efficient catalysis for atmospheric ammonia synthesis, *ACS Nano* 10 (11) (2016) 10507–10515.
- [69] T. Zhao, S. She, X. Ji, W. Jin, A. Dang, H. Li, et al., In-situ growth amorphous carbon nanotube on silicon particles as lithium-ion battery anode materials, *J. Alloys Compd.* 708 (2017) 500–507.
- [70] H. Tang, Y.J. Zhang, Q.Q. Xiong, J.D. Cheng, Q. Zhang, X.L. Wang, et al., Self-assembly silicon/porous reduced graphene oxide composite film as a binder-free and flexible anode for lithium-ion batteries, *Electrochim. Acta* 156 (2015) 86–93.
- [71] S. Tian, G. Zhu, Y. Tang, X. Xie, Q. Wang, Y. Ma, et al., Three-dimensional cross-linking composite of graphene, carbon nanotube and Si nanoparticles for lithium ion batteries anode 29 (2018), 125603.
- [72] M.-I. Jiao, J. Qi, Z.-q. Shi, C.-y. Wang, Three-dimensional Si/hard-carbon/graphene network as high-performance anode material for lithium ion batteries, *J. Mater. Sci.* 53 (3) (2018) 2149–2160.
- [73] W. Sun, R. Hu, M. Zhang, J. Liu, M. Zhu, Binding of carbon coated nano-silicon in graphene sheets by wet ball-milling and pyrolysis as high performance anodes for lithium-ion batteries, *J. Power Sources* 318 (2016) 113–120.

- [74] Q. Wang, T. Meng, Y. Li, J. Yang, B. Huang, S. Ou, et al., Consecutive chemical bonds reconstructing surface structure of silicon anode for high-performance lithium-ion battery, *Energy Storage Mater.* 39 (2021) 354–364.
- [75] Q. Ma, Y. Zhao, Z. Hu, J. Qu, Z. Zhao, H. Xie, et al., Electrochemically converting micro-sized industrial Si/FeSi₂ to nano Si/FeSi for the high-performance lithium-ion battery anode, *Mater. Today Energy* 21 (2021), 100817.
- [76] P. Li, G. Chen, N. Zhang, R. Ma, X. Liu, β -cyclodextrin as lithium-ion diffusion channel with enhanced kinetics for stable silicon anode, *Energy Environ. Mater.* 4 (1) (2020) 72–80.